Chapter 4

Sub-Micron/Nano-Scale Polymorphs of Molybdenum Oxide with Tuned Structural and Morphological Features Embedded in Engineering Thermoplastic
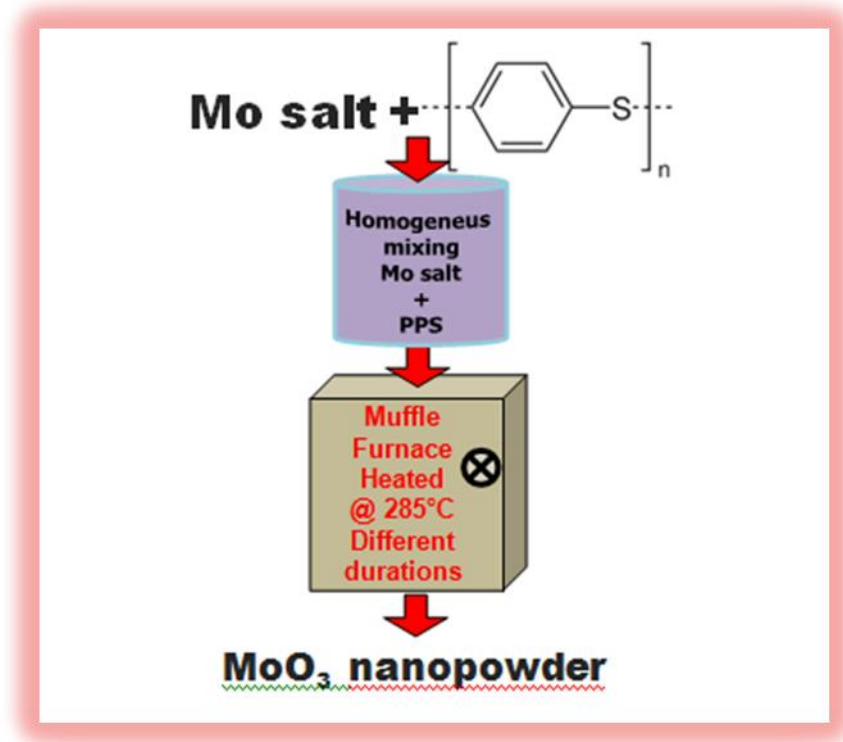
"Success is a science; if you have the conditions, you get the result."

- Oscar Wilde

4.1 Introduction

Nanoscale transition metal and metal oxide structures are attracting continuous attention for a variety of applications, for example, catalysis and modern energy generation and storage systems and devices [1-5]. Among transition metals, molybdenum is cheaper and readily available as compared to the noble metals which can exhibit plasmonic behavior and demonstrate catalytic [6] as well as biosensing applications [7]. Due to its biocompatible nature, it can also be used as an alternative antimicrobial material as compared to silver at the nanoscale. Curiously, research on molybdenum nanoparticles has not been adequately pursued among transition metals both from the synthesis and application point of view. Additionally, molybdenum trioxide is a wonder material discovered over hundred years ago [8] and still surprising the researchers with its novel properties. It is an n-type semiconductor possessing a wide optical bandgap of 3.2 eV. Owing to its superior properties, it is being explored in applications such as catalytic epoxidation of cis-cyclooctene [9] and oxidation of thiophene in the presence of hydrogen peroxide, [10] gas sensing, [10,11] solar cells [12,13] (as anode buffer layer in plasmonic organic solar cells), lithium ion batteries, supercapacitors, [14-18] antibacterial formulations [19], etc. To fully exploit the application potential of these nanocrystals as novel optical and electronic materials, it is important to develop nanocrystals in one dimension or quasi-one dimension, such as nanowires or nanorods, nanoflowers, etc. Moreover, obtaining metal-metal oxide based nanocomposite can be important from the perspective of various technological applications. For example, incorporation of plasmonic noble metals such as gold and silver nanoparticles along with materials such as TiO_2, ZnO, etc for catalytic, environmental and sensor applications have been well-reported [20-22]. The technological applications of metal oxide/metal-metal oxide nanostructured systems can be better realized by providing a flexible yet robust platform/support, viz. preferably embedding it in the polymer matrix. Encapsulation of inorganic nanoparticles in polymers has become one of the most widespread and exciting aspects of nanocomposite synthesis [23]. A variety of polymers, for example, polyaniline and PMMA, have been used for this purpose [24, 25]. However, such engineering thermoplastics as polyphenylene sulfide (PPS) have not been advantageously exploited for nanocomposite systems. In this context, solid–solid reaction technique has been pursued for the synthesis of semiconductor nanostructures in a polymer matrix, [26-29]. Especially, Amalnerkar et al. have done pioneering work in the field of PPS based polymer nanocomposite synthesis [30, 31]. The details of the literature survey corresponding to the synthesis of MoO_3

nanostructures as well as the nanocomposites using solid-solid reaction have already been presented in Chapter 1. However, the proposed technique has not been reported in the domain of Mo-MoO$_3$-PPS and MoO$_3$-PPS nanocomposites. Consequently, the applications of such nanocomposites have also not been explored. Therefore, in this investigation, we examined a simple and innovative technique for *in-situ* generation of Mo-MoO$_3$-PPS and MoO$_3$-PPS nanocomposites having different 1D, 2D and 3D morphologies by solid–solid reaction technique. We have probed the effect of molybdenum precursor and reaction time variation on structural, morphological and optical properties of the prepared nanocomposites in detail.

For the sake of convenience, the present chapter can be divided into three main sections which are summarized as follows:

1) The *first section* details on the preparation of MoO$_3$-PPS nanocomposites (using ammonium molybdate as a precursor by varying the reaction time from 6-48 h) and their exploration in obtaining superior dielectric properties in comparison to PPS.

2) In the *second section* we have dealt with the concurrent *in-situ* formation of Mo- MoO$_3$ nanostructures within an engineering thermoplastic matrix of PPS exhibiting hitherto unreported antibacterial behavior. For this investigation, molybdenum chloride was used as the molybdenum precursor.

3) Molybdenum hexacarbonyl has been used as Mo precursor in the synthesis of MoO$_3$-PPS nanocomposites. The studies pertaining to the synthesis and phsico-chemical characterization have been elaborated in the *third section*.

4.2 Superior Dielectric Performance of Engineering Thermoplastic by *In-situ* Embedding of Nanoscale Mixed Phase Molybdenum Oxide

4.2.1 Experimental

4.2.1.1 Synthesis of nanocomposite powder

All chemicals were of reagent grade and were used as received. Ammonium molybdate and PPS were mixed in a molar ratio of 1:1 in the presence of small amount of acetone for about 20 minutes using mortar and pestle. The resultant admixtures (off white colour) were subjected to heating in a furnace at 285 ˚C (melting point of PPS) for different time durations viz. 6, 24 and 48 h. The furnace was allowed to cool naturally to room temperature as shown in figure 4.1.
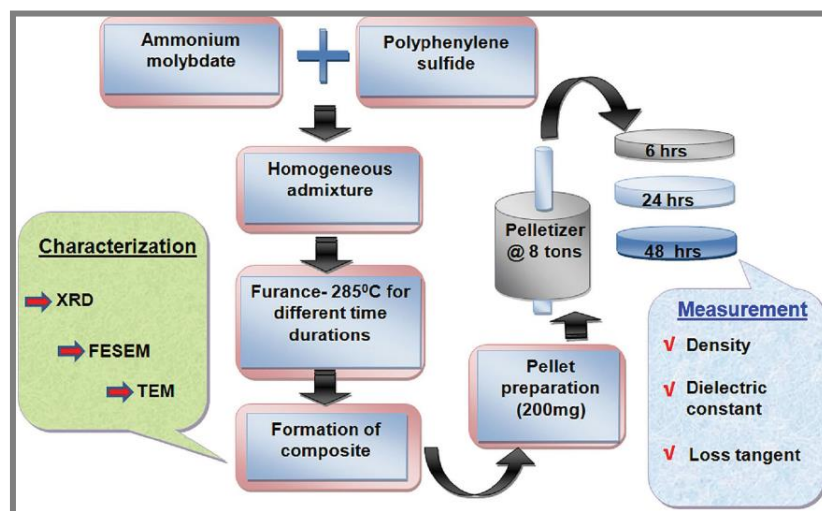
Figure 4.1 *Schematic diagram of synthesis of nanocomposite powder technique*

As the reaction time increased, the color of the resultant powder changed from off-white to dark gray and light gray (figure 4.2) indicating the formation of composites presumably with different compositions and morphologies.
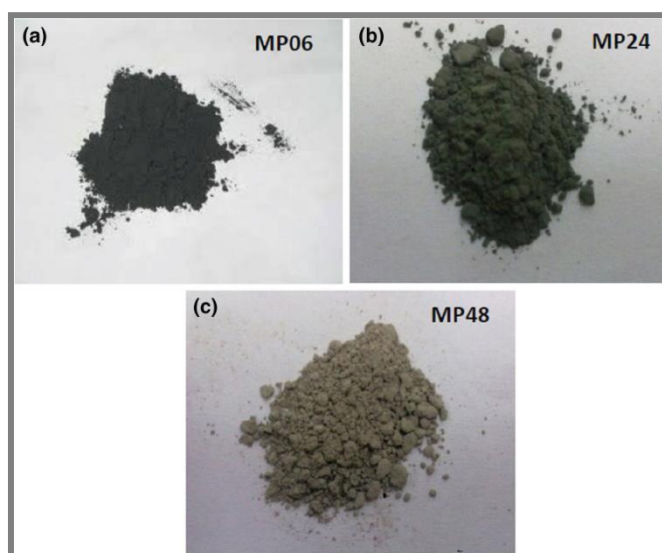
Figure 4.2 *Digital photomicrographs of as prepared powders corresponding to a) MP06, b) MP24 and c) MP48.*

The samples prepared using different reaction times, namely 6 h, 24 h and 48 h were termed as MP06, MP24, and MP48, respectively.

a) Fabrication of nanocomposite in pellet form

Three pellets (200 mg of each) were prepared from the admixed powder by cold pressing using a pelletizer with a pressure of 8 tons. The measured thickness and diameter of the samples were 1.1 mm and 10 mm, respectively.

4.2.1.2 Physico-chemical characterization

a) Structure and morphology determination

The structural information on virgin powder samples was obtained using X-ray diffraction (XRD by Bruker D8 Advance). The surface morphological features on the same were investigated by field emission scanning electron microscopy (FESEM) using a HITACHI S-4800. Microstructural information of sample corresponding to heat treatment of 48 hrs was obtained by transmission electron microscopy (TEM) images acquired on Carl Zeiss Libra 120 EFTEM, 120 KV.

b) Pellet Density Measurement

The theoretical density (ρ_{th}) of the nanocomposite can be calculated using the rule of the mixture as shown in equation 4.1. The densities of MoO_3 and PPS were considered as 5.06 g/cc and 1.34 g/cc, respectively.

$$\rho_{th} = \rho_f V_f + \rho_m V_m \qquad \text{-------------------------------[4.1]}$$

Where, ρ_f is the density of molybdenum oxide particles, ρ_m is the density of polymer matrix, V_f is the volume fraction of molybdenum oxide particles, and V_m is the volume fraction of the matrix. The experimental density (ρ_{ex}) was determined by Archimedes Principle using equation 4.2.

$$\rho_{exp} = \left(\frac{W_{air}}{(W_{air} - W_{liq})} \times \rho_{liq} \right) \qquad \text{-------------------- [4.2]}$$

Where, W_{air} and W_{liq} are the weight of samples in air and liquid medium (ethanol), respectively. The density (ρ_{liq}) of ethanol is 0.79 g/cc. For a comparison, the density of pellet prepared using pure PPS has also been measured.

4.2.1.3 Dielectric characterization

For dielectric measurement, electrodes were prepared by applying the commercial silver paste on both sides of the pellet. The measurements of low-frequency dielectric properties were carried out using an Agilent HP 4192A LF make precession Impedance Analyzer in the frequency range from 1kHz to 15 MHz at room temperature. The dielectric constant (ε) was evaluated using equation 4.3,

$$\varepsilon = \frac{(c \times d)}{(\varepsilon_o \times A)} \qquad \text{--------------------[4.3]}$$

Where, A is the surface area, C is the capacitance, and d is the thickness of the sample. The ε_o is the permittivity of vacuum. The dielectric loss

tangent/ dissipation factor, tan δ is defined as $\dfrac{\varepsilon_r^{"}}{\varepsilon_r^{'}}$ i. e. ratio of imaginary

part of dielectric constant to the real part of dielectric constant and was obtained directly from the instrument.

4.2.2 Results and discussion

4.2.2.1 X-ray diffraction analysis

The X-ray diffractograms for the resultant powders are reproduced in figure 4.3. The XRD patterns predominantly show peaks pertaining to reflections of orthorhombic α-MoO_3 (JCPDS # 05-0508) positioned at 2θ =12.76, 23.32, 25.70, 27.33, 29.69, 33.72, 35.49, 38.97, 46.28, 49.23, 52.77, 55.18, 58.80, 64.52 °, respectively. For MP06 sample, even though orthorhombic MoO_3 is present as the major phase, the diffraction peak at 2θ = 12.76 ° shows the highest intensity. Diffraction peaks corresponding to monoclinic Mo_8O_{23} phase (JCPDS card No. 05-0339) have also been observed (denoted by symbol δ) as the substantial phase in the case of samples MP06 and MP24, respectively. The sample corresponding to heat treatment of 48 h reveals the formation of phase pure orthogonal MoO_3 as all the XRD peaks related to monoclinic Mo_8O_{23} disappear in the sample MP48. The XRD for MP48 is a typical XRD reported for α-MoO_3 with JCPDS # 05-0508 with a weaker peak at 12.76°. The decrease in intensity of the peak at 12.76° for MP06, MP24 and MP48 implies that the conversion of Mo_8O_{23} phase to α-MoO_3 phase has taken place at the cost of a reduction in the intensity of 12.76° peak. Additionally, diffraction peaks corresponding to PPS (at 18.9° and 20.55°) are almost absent for MP48 sample which may be due to cyclization/altering of PPS matrix in the presence of molybdenum precursor after long time heat treatment. The broad peaks are suggestive of nanocrystalline nature of the resultant powder. The typical crystallite size calculated from Scherrer equation is ~ 3 - 8 nm. Relative sharpness of diffraction peaks is observed to be increased in the time variation order of 48 h>24h >6h. The diffraction peaks at 18.9 and 20.55˚ belonging to PPS are observed for MP06 and MP24 samples. From the diffractograms, it is clear that the proposed solid-state reaction involving molybdenum precursor leads to the formation of molybdenum oxides within PPS matrix.
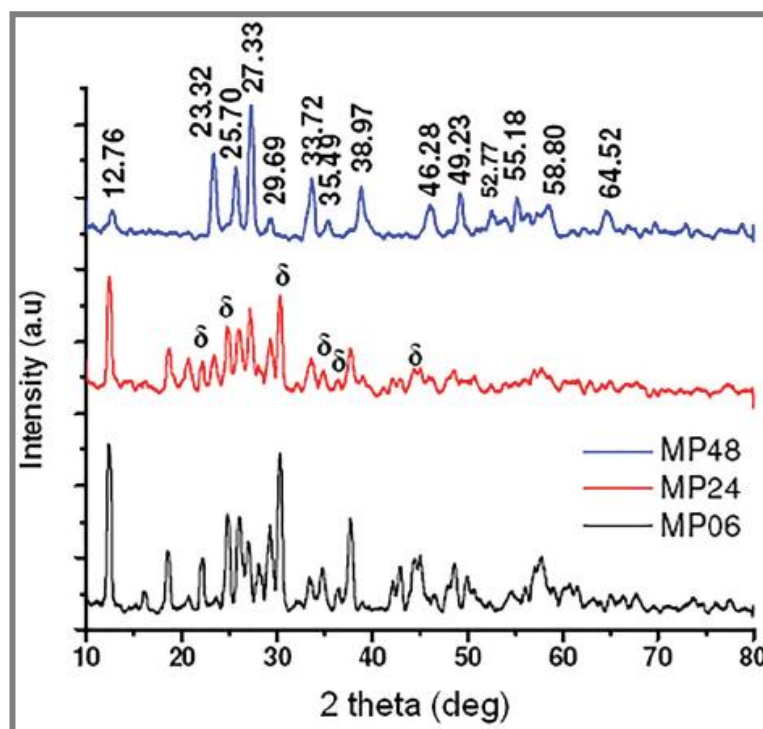
Figure 4.3 *X-ray diffractograms of the resultant powder samples.*

4.2.2.2   Field emission scanning electron microscopy

FESEM images of the resultant powder samples are displayed in figure 4.4. The size of embedded nanoparticles appears to be predominantly irregular along with the presence of a few rod-like structures for sample corresponding to the reaction time of 6 h. The size of irregular nanoparticles varies from ~ 20 – 200 nm. For MP24 sample, irregular strip and sheet-like morphology have been observed. However, 1-D nanoscale strip like nature of obtained structures is the dominant feature for this sample. For the sample corresponding to the heat treatment of 48 h, remarkable sheet-like nanostructures stacked one above another one have been observed. The thickness of the sheet-like structures varies from 20 nm to 40 nm. Thus, at longer reaction times, sheet-like nanostructures have been noticed implying prolonged heat treatment favours the transformation of 0-D and 1-D structures into 2-D along with oxidation.
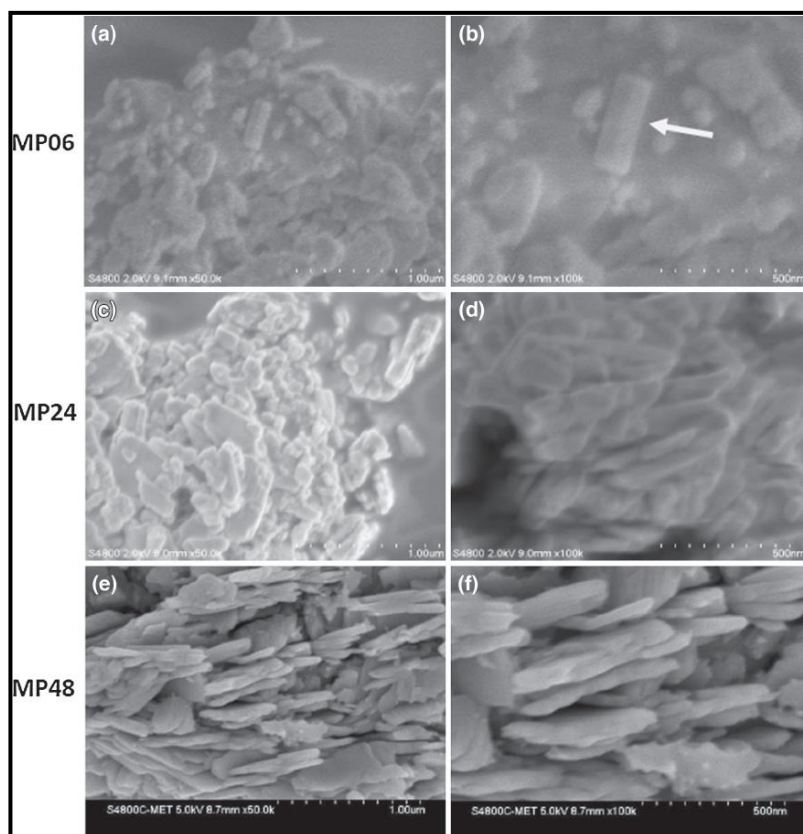
Figure 4.4 *FESEM images of samples - MP06, MP24 and MP48. Images at (a), (c) and (e) correspond to low magnification, and those at (b), (d) and (f) correspond to high magnification, respectively.*

4.2.2.3 Transmission electron microscopy

In order to ascertain the microstructure of the resultant nanocomposite, representative TEM images of the resultant powders corresponding to 48 hrs of reaction were obtained and shown in figure 4.5. The TEM images disclose the predominant formation of sheet-like nanostructures. From low magnification (figure 4.5a) and high magnification (figure 4.5b) images, it appears that the sheet-like structures is formed and stacked one above another one. In this context, it is worthwhile to note that orthorhombic α-MoO$_3$ belongs to the family of layered structures [32]. Thus, as the intensity of the peak at 27.33° corresponding to α-MoO$_3$ increases, more tendency to form sheet-like 2-D structures is observed. Additionally, during the growth, PPS in molten form may provide suitable nucleating sites for heterogeneous growth leading to the formation of such sheet-like structures. These sheets like structures correlate well with the similar structures observed in TEM images for this sample.
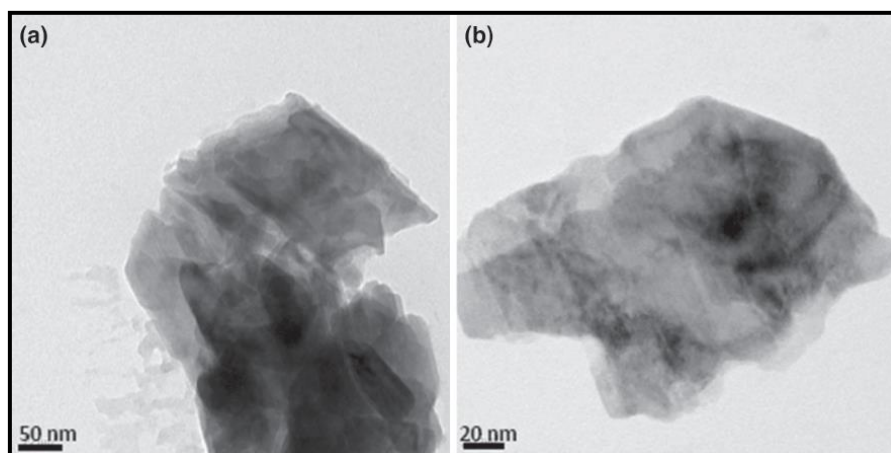
Figure 4.5 *The TEM images of MP48 sample (a) low magnification and (b) high*
magnification.

4.2.3 Dielectric properties studies

a) Density of nanocomposites

The values of the densities have been calculated using the equation (4.1) &
(4.2), and for comparison, the density of pure PPS has also been calculated.
The densities of all the samples MP06, MP24 & MP48, were almost the
same. Therefore the description of the density of only one sample has been
included in the text. It may be noted that 285 °C is the melting temperature
of PPS. The degradation of PPS takes place at a further higher temperature
(above 400 °C). At 285 °C, during the present reactions, as the reaction time
increases, cyclization of PPS takes place, and its loses its crystalline nature
leading to the decrease in the intensity of peaks corresponding to PPS.
However, PPS does not degrade as the reaction is taking place well below
its degradation temperature. Due to this, the density of all the samples
remains almost unaltered. The experimental density of nanocomposite is
observed to increase from 1.34 g/cc for pure PPS to 2.35 g/cc for PPS-
molybdenum oxide nanocomposite. It is obviously due to the higher density
of molybdenum oxide.

b) Dielectric Properties

Figure 4.6 shows the plots of dielectric constant of molybdenum oxide
nanocomposites as a function of frequency. With the increase in applied
frequency, dielectric constant of nanocomposites was found to be
decreased. Molybdenum oxide is an inorganic material, and when a high-
frequency AC field is applied, the molybdenum oxide nanostructures are in a
quick and weak polarization state which may result in a lower dielectric
constant for the nanocomposite at higher frequencies. The increase in
dielectric constant of the PPS/molybdenum oxide nanocomposites in the

low-frequency region can be attributed to the contribution from space charge polarization effect. Figure 4.6a shows the typical performance of dielectric constant over a wide range of frequencies, up to 15 MHz. The dielectric constant decreases rapidly in the frequency range of 1kHz to 100 kHz. The highest dielectric constant is obtained for MP06 sample in the low-frequency region up to 100 kHz. Sample MP24 displayed the lower values of dielectric constant in this range. However, in the high-frequency region above 100 kHz (figure 4.6b), sample MP24 exhibits relatively higher dielectric constant compared with MP06 and MP48. The dielectric constant in low and high-frequency region is dependent on the contribution of polymer, filler, and their interaction regions. It is speculated that polymer and filler-polymer interaction dominates for sample MP24 and thus it shows a higher dielectric constant.
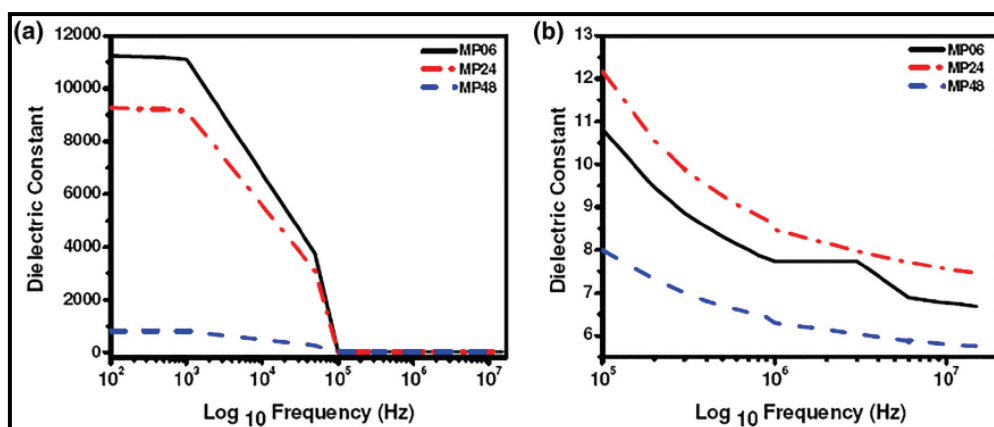
Figure 4.6 *Frequency versus dielectric constant behaviour of MoO$_3$-PPS nanocomposites (a) from 100 Hz to 15 MHz and (b) from 100 kHz to 15 MHz*

The dissipation factor (loss tangent or tan δ) also show the similar trend over the same range of frequencies, as shown in figure 4.7. However, in the high-frequency region above 100 kHz (figure 4.7b), sample MP48 has shown the lowest values of dielectric loss tangent. Samples MP06 and MP24 have similar dielectric loss tangent values in this range. For samples MP06, MP24 and MP48, the dielectric constant and loss tangent are found to be 7.74, 8.47, 6.30 and 0.14, 0.13, 0.089, respectively, at 1 MHz frequency. Even though the MP24 sample shows better dielectric constant at 1 MHz frequency, its higher loss tangent value may limit its application in the capacitor. It may be noted that the obtained dielectric constants for the resultant nanocomposites are more than double of the reported values of pure PPS [33] with a fairly better loss tangent value. Especially, sample

MP48 will be more suitable for the application in the range of 100 kHz to 15 MHz as it has better dielectric constant and lower loss tangent values than those of other samples in this frequency range. It exemplifies the outstanding characteristics of low dielectric constant and dissipation factors.
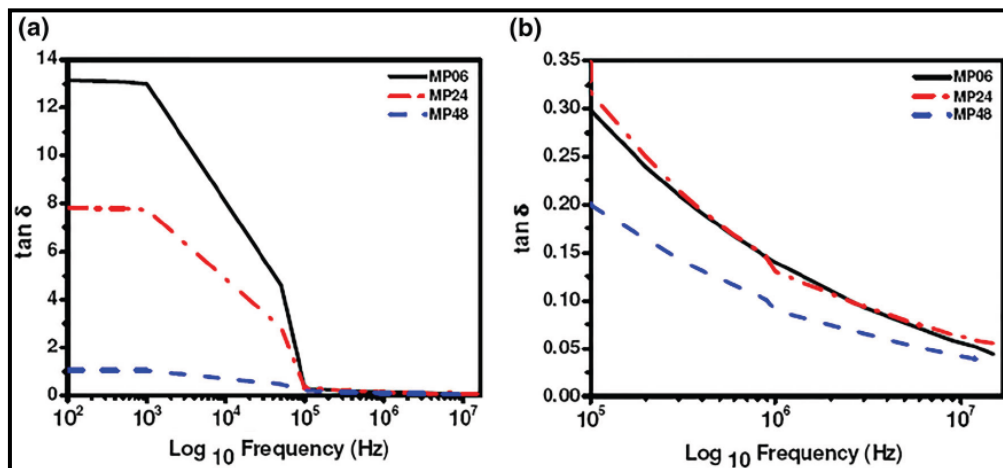
Figure 4.7 *Frequency versus dissipation factor of MoO$_3$-PPS nanocomposites (a) from 100 Hz to 15 MHz and (b) from 100 kHz to 15 MHz.*

4.2.4 Summary

In-situ synthesis of molybdenum oxide nanostructures in an engineering thermoplastic has been accomplished using a facile solid-solid technique. As the reaction time is increased from 6 to 48 h, the tendency of forming 2-D sheet-like structures is found to be enhanced. Investigations on dielectric properties are the salient aspect of this work which reveals better dielectric constant and appreciable loss tangent values for the resultant nanocomposites. The first envisaged application for these nanocomposites may be capacitors for high power, high temperature (up to 125 °C) AC field and surface mount circuits. The obtained nanocomposite may also be useful for various flexible radio frequency identification (RFID) tag-based applications such as access control, smart cards, and library control as well as energy storage related devices and systems. Gas sensing and biosensing might be another anticipated applications for these nanocomposites.

4.3 Sub-micro/nano-scale Polymorphs Of Molybdenum Oxide With Tuned Structural And Morphological Features Embedded In Engineering Thermoplastic

4.3.1 Experimental

4.3.1.1   Synthesis of molybdenum oxide in PPS matrix

All chemicals were of reagent grade and were used as received. The precursors, molybdenum hexacarbonyl, and PPS were admixed in 1:1 molar ratio in agate mortar and pestle. A few drops of acetone were added for proper wetting of the reactants. The admixture thus formed was then heated to the melting temperature of the polymer (at 285 °C) for variable time intervals such as 6, 12, 24, and 48 h in a muffle furnace under normal atmospheric conditions. The furnace was allowed to cool naturally to room temperature. The corresponding samples are named as Sample A, Sample B, Sample C and Sample D corresponding to reaction times of 6, 12, 24 and 48 h, respectively. The experimental procedure is depicted in figure 4.8. The color of the resultant powder was changed from black to light gray with an increase in the time interval.
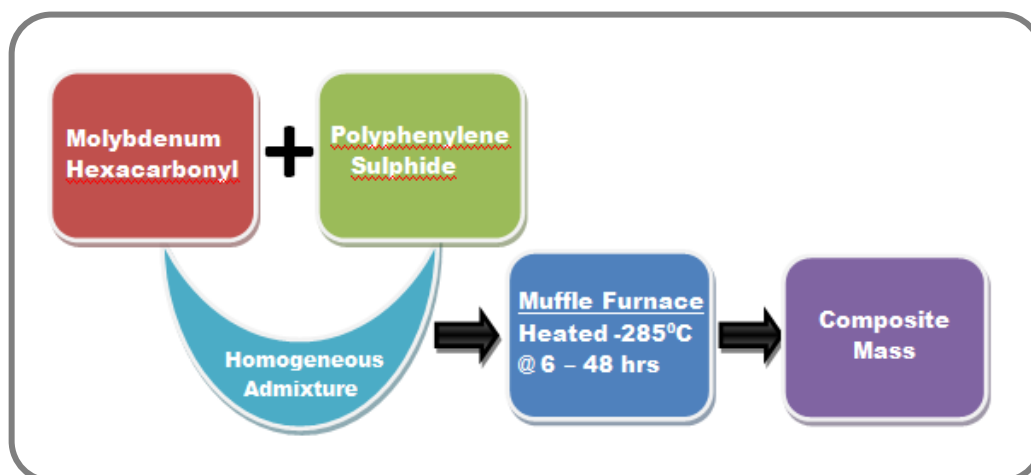
Figure 4.8 *The experimental procedure of MoO$_3$-PPS*

4.3.1.2 Physico-chemical characterization

The resultant products were characterized by techniques namely, X-ray diffractometry (XRD), Raman spectroscopy, field-emission scanning electron microscopy (FESEM) and high resolution transmission electron microscope (HRTEM). The phase identification of the resultant powder was conducted using X-ray diffractometer (Brucker D8 Advance), using CuKα radiation (λ = 1.54 Å). Raman spectroscopy has been performed using DXR Raman Microscope (Thermo Scientific), Laser wavelength: 532 nm, spectral resolution: 2 cm^{-1} for high resolution grating, 5 cm^{-1} for full range grating and laser power of 1-10 mW. The surface morphology was determined using FESEM, Hitachi S-4800 by directly placing the solid samples on conducting carbon tape. In order to prevent the charging effect associated with FESEM, the samples were sputter coated with a thin Au film. The microstructure of the samples was investigated by

HRTEM with Tecnai G^2-20U-Twin (FEI, Netherlands), at an acceleration voltage of 200 KV. The samples for HRTEM were prepared by dispersing fine powder of the resultant product in isopropyl alcohol. A drop of dispersion was then transferred to carbon coated grid for further analysis.

4.3.2 Results and discussion

4.3.2.1 Reaction mechanism

Molybdenum hexacarbonyl is highly volatile and may decompose to form metallic Mo and carbon monoxide upon heat treatment. The metallic Mo will undergo oxidation when it comes in contact with hot air. The PPS matrix may provide the suitable heterogeneous nucleation sites for the formation and faceted growth of molybdenum oxide. For the longer reaction times, the growth process will dominate leading to the formation of bigger structures.

$$Mo(CO)_6 + \left[\langle\!\bigcirc\!\rangle\!-\!S\right]_n \xrightarrow{\text{285 °C}} Mo + 6\,CO\uparrow \xrightarrow{\text{285 °C}} 2Mo + 6O_2 \xrightarrow{\text{285 °C}} 2MoO_3.$$
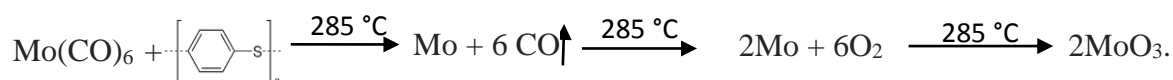
4.3.2.2 X-ray diffraction

The XRD patterns obtained for the resultant products are reproduced in Figure 4.9. The XRD patterns in figure 4.9 corresponding to Sample A, Sample B, Sample C and Sample D indicate the predominant formation of orthorhombic phase of α-MoO$_3$ (JCPDS Card No. 05-0508). It is worthy to note that the diffraction peak observed at 2θ value of 20.5° (figure 4.9) matches with the prominent peak of PPS [34]. The X-ray diffractogram corresponding to Sample A reveals broad peaks with a preferred orientation along (021) plane of α-MoO$_3$. It also exhibits relatively higher intensity for the (110) plane. The peak broadening implies the formation of nanocrystalline structures. Additionally, few low-intensity peaks corresponding to monoclinic Mo$_8$O$_{23}$ phase (JCPDS card No. 841360) have also been observed (denoted by symbol δ). In the case of Sample B, even though sharp peaks corresponding to α-MoO$_3$ are detected, they are preferentially oriented around (040) plane; peak intensity corresponding to (021) plane is significantly reduced. Additionally, peak intensity around (130) plane (which is otherwise a minor intensity peak in standard diffraction data of α-MoO$_3$) is also appreciably increased. The absence of low-intensity peaks corresponding to minor phases implies that phase pure α-MoO$_3$ is formed. However, a very interesting situation arises in the case of Sample C. Considerable increase in the intensity of the peak corresponding to (020)

plane is observed with a drastic reduction in intensities pertaining to (021) and (110) planes. There is significant increase in peak intensities corresponding to monoclinic Mo_8O_{23} phase (JCPDS card No. 84-1360). XRD pattern for Sample D reveals the formation of phase pure α-MoO_3. However, the plane corresponding to (021) exhibits the highest intensity peak in this case. Peak intensity corresponding to (020) plane is decreased noticeably. Besides, the sharpness of the peaks has also increased indicating the growth in particle size. Highly suppressed peak corresponding to PPS is noticed which may be due to cyclization of PPS over prolonged heat treatment.
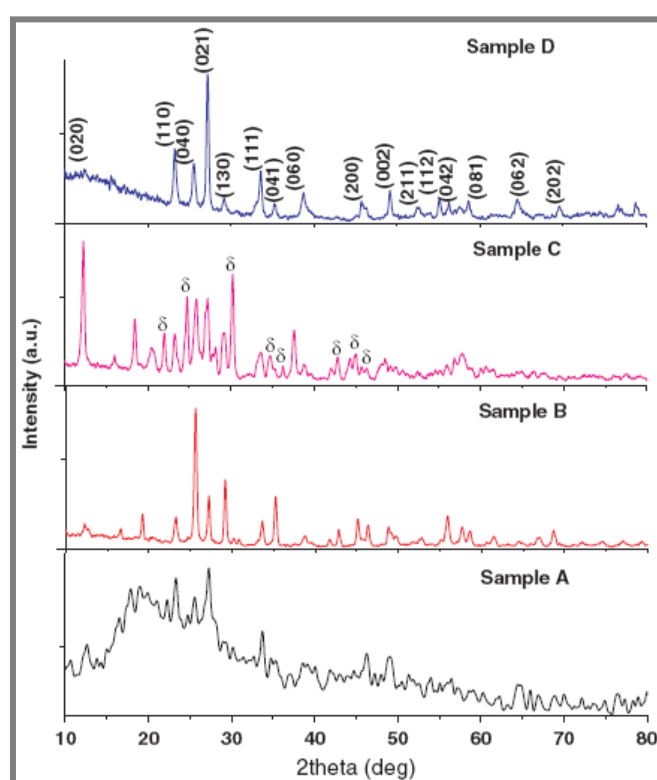
Figure 4.9 *XRD patterns of Sample A, Sample B, Sample C, and Sample D.*

Crystallite size calculated using Scherer formula is found out to be ~ 12 - 20 nm for Samples A to D corresponding to their highest intensity peaks. Nevertheless, relative sharpness of diffraction peak is observed to be enhanced with the time variation order of 48 h>24h >12h>6h. This may be attributed to the increase in crystallinity and grain size. From the XRD analysis, it is inferred that the proposed solid-state reaction involving molybdenum precursor leads to the formation of molybdenum oxide within PPS matrix. It is conjectured that since each sample has a differentially oriented highest intensity plane, it will influence the resultant morphology of the entrapped sub-micron/nanoscale polymorphs of molybdenum oxide.

4.3.2.3 Field emission scanning electron microscopy

FE-SEM images for the resultant composites are displayed in figure 4.10 (a)–(d). FE-SEM images of samples corresponding to 1:1 molar ratio of Mo salt: PPS with different reaction intervals (6-48 hr) elucidate formation of molybdenum oxide sub-micro/ nanoscale particles embedded within the PPS matrix possessing mixed morphologies such as rods, sheets, and cubes. The information pertaining to the morphological features obtained from the FESEM images is summarized below:

(i) For Sample A, the formation of spherical and irregular shaped nanostructures is noticed. Occasionally, nanorods like structure have been found to be formed. One such hexagonal nanorod-like structure is displayed in figure 4.10a. The length of this nanorod is around 300 nm and its thickness is ~100 nm.

(ii) The FESEM image for the Sample B reveals the formation of the irregular rod, sheets like structures (figure 4.10b). Particle size is found to be increased. A predominance of irregularly shaped particles is clearly visible. An irregular disk-shaped particle displayed in figure 4.10b is ~350 nm wide and 150nm long. The particle size of some nanostructures varied in the range of 50 to 100 nm.

(iii) In the case of Sample C, cubic block and rectangular brick-like structures are noticed primarily (figure 4.10c). The length of these submicron structures vary from 300 nm to 600 nm and thickness varies from 100–300 nm. Additionally, small rod and cube like nanostructures have also been observed along with irregularly shaped nanostructures.

(iv) FESEM image pertaining to Sample D (figure 4.10d) display reverse L-shaped sub-micron sized structures. Two such reverse L-shaped structures have been displayed in figure 4.10d.

Interestingly, as reaction time is increased from 6-48 hrs, more number of rod and sheets like structures have been noticed implying that prolonged heat treatment favours 1-D and 2-D growth during oxidation. Formation of such interesting morphologies may be correlated to the XRD data. For the Samples (A and D), planes corresponding to (021) possessed the highest intensity which has lead to the formation of submicron/nanostructures having rod-like morphology (figure 4.10a & 4.10d). Thus, it may be speculated that (021) plane for the orthorhombic phase of MoO_3 favor formation of rod-like morphology. Sample B (figure 4.10b) which has exhibited the highest intensity peak around (040) plane, irregular hexagonal

disk-like morphology is revealed in FE-SEM hinting that growth along (040) plane supports the formation of such structures. Sample C has displayed preferred orientation along (020) plane in XRD and formation of cubic and rectangular brick-like structures in FESEM (figure 4.10c). It implies that (020) plane obstructed the growth along (021) plane leading to the formation of 3-D brick-like structures instead of 1-D rod-like structures.
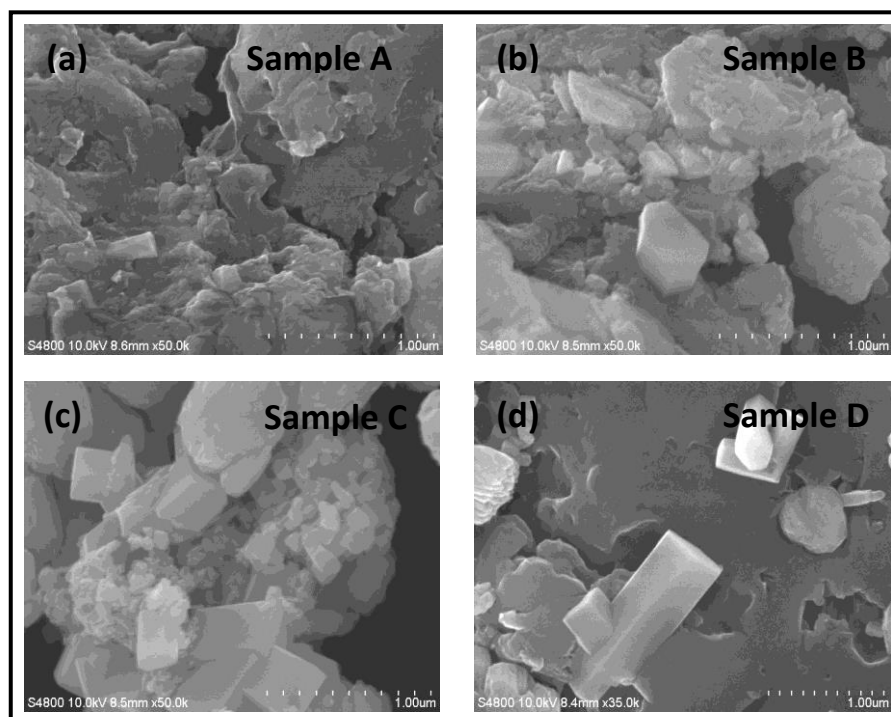
Figure 4.10 *FESEM images of the resultant powders corresponding to (a) Sample A, (b) Sample B, (c) Sample C and (d) Sample D.*

4.3.2.4 High resolution transmission electron microscopy

In order to ascertain the micro-structural features of molybdenum oxide nanocomposite, the representative HRTEM imaging has been performed for Sample A and Sample D. HRTEM images corresponding to the reaction time of 6 hr (Sample A) have been shown in figure 4.11. Typical low magnification HRTEM image (figure 4.11a) displays the formation of nanostructures having rod-like as well as irregular shapes within the PPS matrix. The rod-like structure has a thickness of around 100 nm and length more than 500 nm. At high magnification (figure 4.11b), the nanorod structure shows crystalline nature. The lattice spacing of 3.78 Å matches well with the 3.71 Å ascribed to (200) plane of Mo_8O_{23}. The inset of figure 4.11b shows a regular matrix of dark spots indicating the single crystalline nature of the nanorod structure.
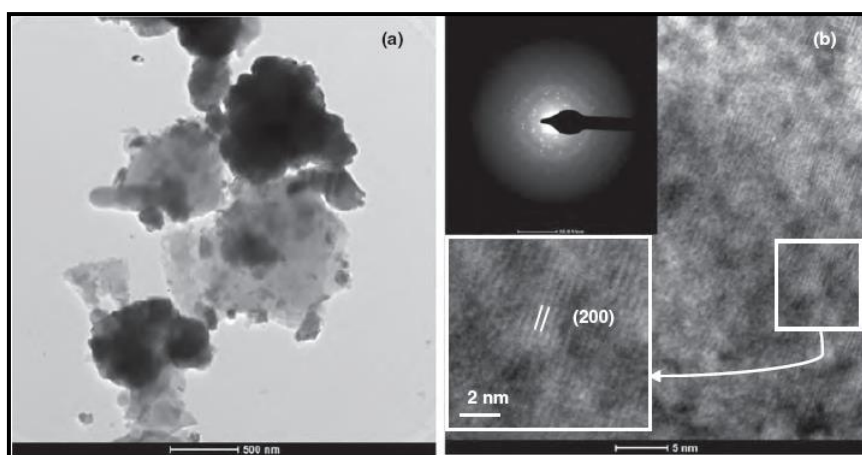
Figure 4.11 *HRTEM images of Sample A at (a) low magnification and (b) high magnification (Inset: SAED pattern).*

HRTEM images corresponding to the reaction time of 48 hr (Sample D) have been shown in figure 4.12. The low magnification image (figure 4.12a) shows the predominant formation of rod-like structures having various sizes. The biggest of such nanorods has the length ~1 μm and thickness of ~ 400 nm. At higher magnification, an edge of a smaller nanorod shows crystalline nature. The lattice spacing value is found out to be 3.17 Å which connect well with the 3.25 Å reported for (021) plane of α-MoO_3. The inset of figure 4.12b shows a regular matrix of dark spots indicating the single crystalline nature of the nanorod structure. Thus, the HRTEM images correlate well with observed HRSEM images. HRTEM images of the representative samples (Sample A and Sample D) reveal the formation of mainly crystalline nanorod-like products. Additionally, as the reaction time is increased, the dimensions of the nanorods have also increased (reaching even up to submicron to micron sizes).
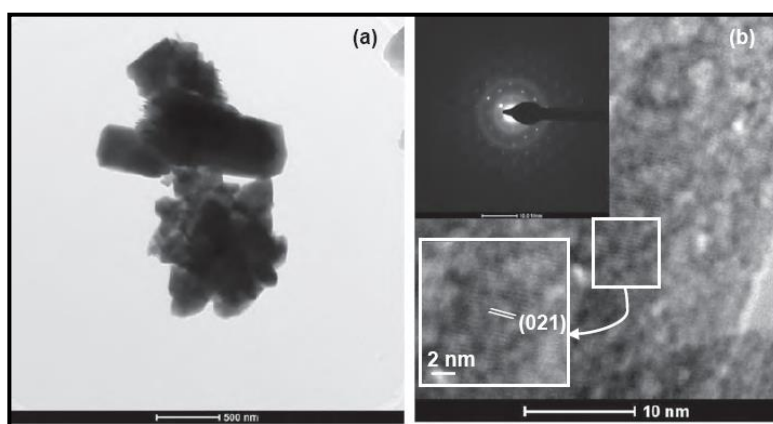
Figure 4.12 *HRTEM images of Sample D at (a) low magnification and (b) high magnification. (Inset: SAED pattern).*

4.3.2.5 Raman spectroscopy

Raman spectra corresponding to all the samples have been presented in figure 4.13. The spectra evince formation of predominantly α-MoO$_3$ via the characteristic peaks in the region of 100 – 1000 cm^{-1}. Two broad humps which center around 1500 and 2000 cm^{-1} may be attributed to the PPS. However, such humps are observed to be less prominent in the case of Sample D which may be due to increased cyclization of PPS after prolonged heat treatment of 48 hrs. For a better understanding of the Raman spectra, the enlarged Raman spectra for the region of 50 – 1000 cm^{-1} have been reproduced in figure 4.13b. The Raman peak positions at 994, 818, 662, 375, 336, 285, 246, and 157 cm^{-1} can be typically assigned to the orthorhombic phase of α-MoO$_3$ [32]. Relatively sharper peaks in the Raman spectrum of MoO$_3$ signify the highly crystalline nature along with the better structural order in MoO$_3$ micro/nanostructures prepared at 48 hrs of reaction time. Comparatively broader peaks and increase in the intensity of baseline for other Samples (A, B, and C) may be allocated to smaller particle size and presence of another minority phase (monoclinic Mo$_8$O$_{23}$) and higher presence of PPS matrix. It may be noted both Sample A and Sample D have exhibited the highest intensity for the peak at 818 cm^{-1} which is coincidently the highest intensity Raman spectrum peak for α-MoO$_3$ [32]. The intensity of Raman peak at 994 cm^{-1} is conspicuously reduced for Sample B and Sample C (almost absent). Additionally, for Sample C, the sharp peak has appeared at 962 cm^{-1} which may be due to the presence of the minority phase. The Raman spectroscopy results are in conformity with certain facts reflected in XRD. For example, increase in the intensity of Raman peak at 818 cm^{-1} coincides with the increase in the intensity of the XRD peak for (021) plane. Also, absence/reduction in intensity of the peak at 994 cm^{-1} coincides with an increase in the intensity of (020) and (040) planes.
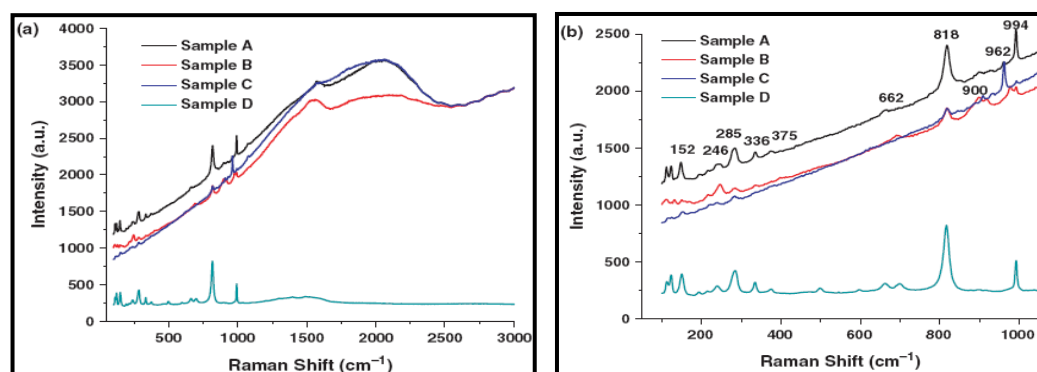
Figure 4.13 *Raman spectra corresponding to Samples A, B, C and D.*

4.3.3 Summary

We have successfully synthesized submicron/nanostructures of molybdenum oxide polymorphs intractable polymer matrix by facile solid-solid reaction technique. The predominant formation of orthorhombic α-MoO₃ was confirmed by structural analysis. It has been observed that the morphology (from 1-D to 3-D) and structure of the resultant polymorphs can be suitably tuned by changing the reaction interval. This could be advantageous from the standpoint of morphology and structure based device fabrication. The polymer, PPS being an engineering thermoplastic with inherent flame retardant characteristics can be molded as desired for fabrication of advanced devices which can be operated at moderately high temperature. Owing to the coupling of desired characteristics of both molybdenum oxides and PPS in the form of submicron/nanocomposites can be advantageously exploited in advanced solid state device fabrication which operates at a moderately higher temperature (up to 200 °C) such as capacitors and sensors.

4.4 Nano-scale Mo-MoO₃ Entrapped In Engineering Thermoplastic: Inorganic Pathway To Bactericidal And Fungicidal Action

4.4.1 Experimental:

4.4.1.1 Synthesis of molybdenum oxide

All the reagents were of analytical grade and used without further purification. In the present work, Mo and MoO₃ nanostructures are simultaneously generated within polyphenylene sulfide (PPS) matrix via solid state reaction between MoCl₃ (Alfa Aesar) and PPS (Aldrich Chemicals). PPS acts as a stabilizing agent for the generated nanoparticles [35]. In a typical procedure, MoCl₃ and PPS are mixed homogeneously in a known molar ratio (1:1) in a pestle mortar using acetone. The resultant admixtures are kept in a furnace for 6h, 24h, and 48h at melting temperature of PPS i.e. 285°C and finally allowed to cool naturally to room temperature. The as-prepared powder samples corresponding to reaction times 6h, 24h and 48h (denoted as N6, N24, N48) display different colors such as blue, gray and black for the reaction time of 6h, 24h, and 48h, respectively. The powders thus obtained were in the form of bigger chunks which could be easily crushed to a fine powder using pestle-mortar.

4.4.1.2 Physico-chemical characterization

The structural information on virgin powder samples was obtained using X-ray diffraction (Bruker D8 Advance) technique. The diffraction angle (2θ) was varied between 10 - 80° range and the observed XRD peaks were

compared with standard JCPDS data. The surface morphological features were investigated by field emission scanning electron microscopy (FESEM) using HITACHI S-4800 instrument. The microstructural aspects of the samples were examined by high resolution transmission electron microscopy (HRTEM) with Tecnai G^2-20U-Twin instrument (FEI, Netherlands) at an acceleration voltage of 200 KV. The samples for FETEM were prepared by dispersing fine powder of the resultant product in isopropyl alcohol. A drop of dispersion was then transferred to carbon coated grid for further analysis.

4.4.1.3 Antimicrobial activity study

Primary antimicrobial activity was ascertained by studying the zone of inhibition. It was followed by determining minimum inhibitory concentration (MIC) and minimum bactericidal/fungicidal concentration (MBC/MFC). MIC and MBC/MFC are the lowest concentrations (of NCs, in the present case) at which a tested compound inhibits growth or kills more than 3 logs (99.9%) of microorganisms. The lowest concentration of NCs showing visual growth inhibition was considered as the MIC. All MIC and MBC values were based on experimental repeats in triplicate. Finally, time kill assay was performed against the NCs sample showing the highest MBC value.

a) Zone of inhibition

All the NCs samples were sonicated in 10% DMSO and used for further investigations. The antibacterial and antifungal activity of the resultant nanocomposites (NCs) was judged against selected microorganisms by determining the diameter of inhibition zone (DIZ) in agar well diffusion test. DIZ reflects the magnitude of susceptibility of the microorganism. The concentrations used for antimicrobial assay were varied in the range of 25, 50, 75, 100 and 500 µg/well.

b) Minimum inhibitory concentration (MIC)

MIC was determined by exposing the micro-organisms to the predetermined concentrations of NCs. Micro-organisms were grown in Mueller Hinton (M-H) broth comprising various concentrations of NCs and 10^5 CFU/ml of bacterial cells at 37 °C in an incubator shaker (REMI CIS – 24 Plus) with shaking speed of 150 rpm for 24 h. The final concentrations of NCs used in the experiment were 0.2, 0.4, 0.6, 0.8, 1.0 and 1.5 mg/ml.

c) Minimum bactericidal / fungicidal concentration (MBC/MFC)

The possibility of misinterpretation of the results due to the turbidity of insoluble compounds, if any, in determining the MBC was avoided by sub-

culturing the above MIC serial dilutions in freshly prepared nutrient agar plates and incubation at 37 °C for 48 h. MBC was regarded as the concentration of the NCs that did not show any growth on a new set of agar plates due to the prevention of the bacterial colony growth on this solid media.

d) Time Kill Assay

Time-kill curve was used to analyze post-treatment bacterial viability and to define the minimum time necessary to reach an inhibitory or bactericidal effect. Examination of the growth curves of bacterial cells was accomplished using *Staphylococcus aureus* through the time kill assay. The cells of *S. aureus* were exposed to NCs via M-H broth at different concentrations (1/2 MIC, MIC, and 2MIC) of NCs. Bacterial concentration was adjusted to 10^5 CFU/ml and each culture were incubated in a shaking incubator at 37 °C. Growth curves of bacterial cell cultures were calculated through repeated measure of the optical density (O. D.) using ELICO SL 210 double beam U-V visible spectrophotometer at 600 nm.

4.4.2 Results and discussion

4.4.2.1 Reaction mechanism

MoCl$_3$ is known to melt/decompose at 410 °C, however, in the present reaction, the temperature was maintained at 285 °C, the melting point of PPS. Since MoCl$_3$ is homogeneously admixed in the PPS matrix, PPS may act as a catalyst reducing the decomposition temperature of MoCl$_3$ from 410 °C to 285 °C or below. PPS also acts as a capping agent preventing the oxidation of Mo. However as the reaction time increases, oxidation of Mo begins to take place due to partial degradation of PPS.

$$2MoCl_3 \xrightarrow[\text{PPS}]{\text{6-24h}} 2Mo + 3Cl_2 \xrightarrow{\text{48h}} Mo + MoO_3$$
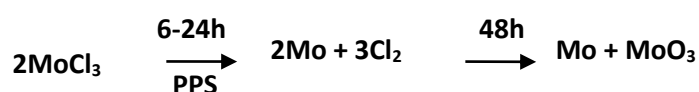
4.4.2.2 X-ray diffraction

Figure 4.14 presents the typical XRD patterns of the as-prepared samples (N6, N24, and N48) which indicate the predominant formation of cubic phase of metallic molybdenum (JCPDS card no.42-1120) and a minor phase of monoclinic MoO$_3$ (JCPDS card no. 85-2405). As the reaction time increases, the resultant samples show little change in the relative intensity or sharpness for peaks corresponding to metallic molybdenum. However, the peak intensities were found to increase for molybdenum trioxide as reaction time increased from 6h to 48h. Especially, peak intensity around (011) plane (which is a minor intensity peak in monoclinic MoO$_3$) was also

appreciably increased with increase in the reaction time. It may be speculated that the molybdenum (100) surface provided suitable nucleation sites for the growth of (011) MoO_3 plane. From the diffractograms, it is evinced that the proposed solid-state reaction involving molybdenum precursor leads to the formation of metallic molybdenum and semiconducting molybdenum oxide within PPS matrix. It is conjectured that as the reaction time increases, metallic molybdenum gradually oxidizes to molybdenum oxide.
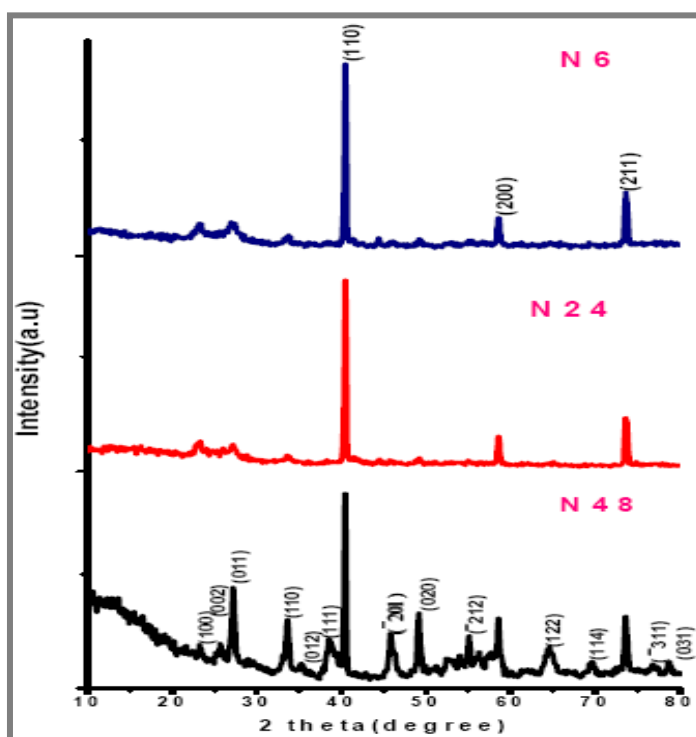
Figure 4.14 XRDs corresponding to samples N6, N24 and N48.

4.4.2.3 Field emission scanning electron microscopy

 FESEM images of the resultant composites samples are displayed in figure 4.15 (a)–(f). FESEM images of samples corresponding to 1:1 molar ratio of Mo salt: PPS prepared with different reaction intervals (6h-48h) elucidate nanoscale formation of molybdenum/molybdenum oxide embedded within the PPS matrix possessing mixed morphologies such as rods, sheets as well as spherical and irregular particles. The information pertaining to the morphological features obtained from the FESEM images for each sample is summarized below: (i) For sample N6, the formation of spherical and irregular sheet-shaped nanostructures was noticed as displayed in figure 4.15a and b. The size of the spherical nanostructures was ~ 20-40 nm and irregular sheet nanostructures varied from ~100-400

nm in size. (ii) The FESEM images for the sample N24 reveals the generation of irregular sheet-like structures (figure 4.15c and d). A predominance of irregularly shaped sheets was clearly visible. The size of the sheet-like structure is found to be increased as compared to that of the sample N6. The irregular shaped nanostructured sheets displayed width varying from ~ 100-800 nm and were observed to be ~10-30 nm thick. (iii) Hierarchically entangled sheets like nanostructures were
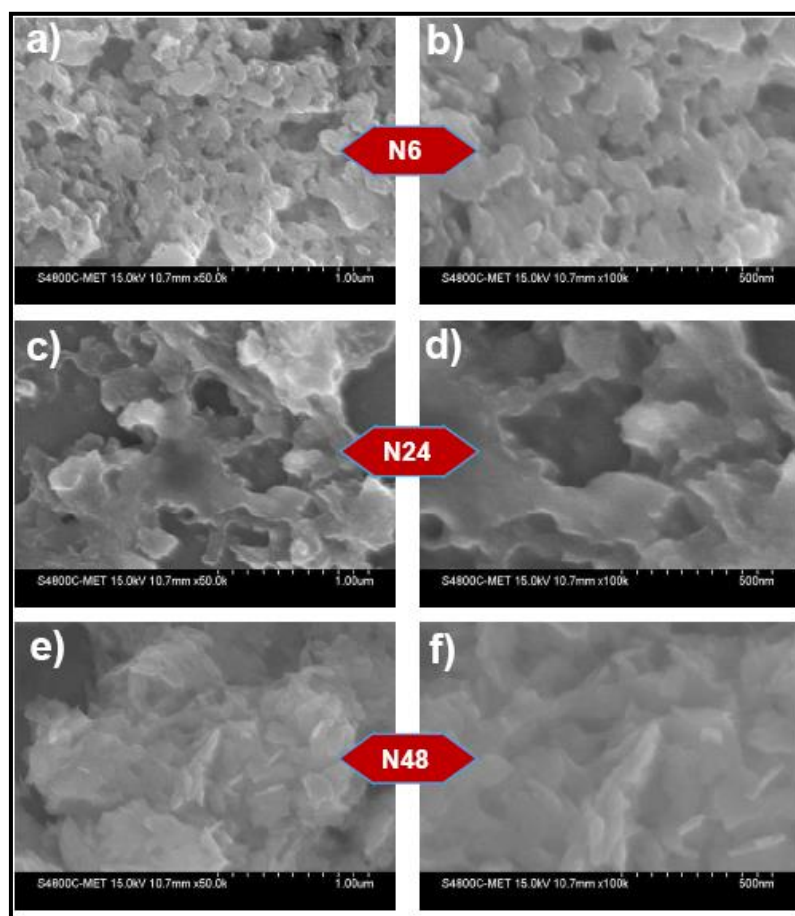
Figure 4.15. *FESEM images of the resultant powders corresponding to lower magnification (a, c, e) and, higher magnification. (b, d, f) for samples N6, N24 and N48, respectively*

detected in the case of sample N48 (figure 4.15e and f). The width, as well as thickness of sheets, decreased as compared to other samples, and it was observed that these sheets tend to self-assemble forming complex hierarchical nanostructures. The width of these nanosheets varies from 100 nm to 200 nm and thickness varies from 10–20 nm. Interestingly, as reaction time was increased from 6h–48h, number of nanosheet-like structures have been noticed implying that prolonged heat treatment favors 2-D growth.

4.4.2.4   High resolution transmission electron microscopy

HRTEM images of the resultant samples are reproduced in figure 4.16. The gist of micro-structural information for the NCs is as follows: (A) The HRTEM image corresponding to sample N6 (figure 4.16a, at low magnification) showed the formation of sheet-like structures. The width of the sheets varied from 20 nm-50 nm, while the length varied from 50 nm-120 nm. Higher magnification image obtained on a representative sheet (figure 4.16b) revealed crystalline structure. The recorded lattice spacing of 0.232 nm matched well with d-spacing corresponding to (110) plane of cubic metallic molybdenum.
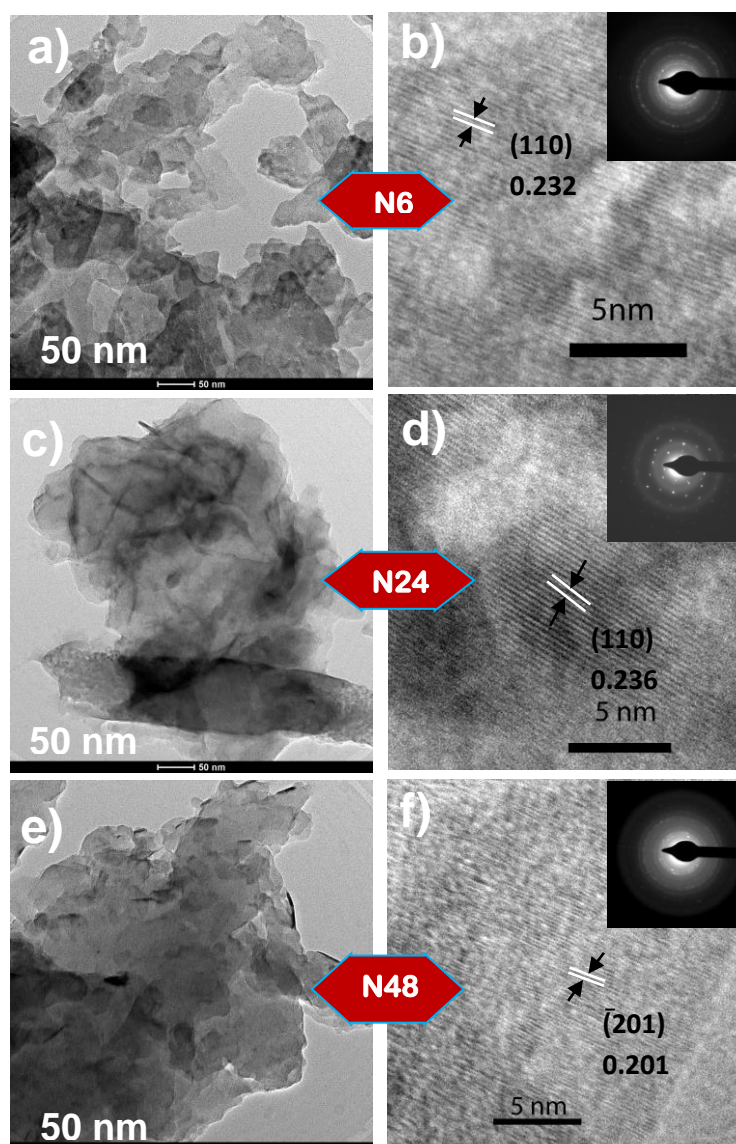
Figure 4.16 *The higher (b, d, f) and lower (a, c, e) magnification HRTEM images of the resultant NCs corresponding to N6, N24 and N48 samples, respectively.*

The inset of the figure 4.16b represents the selected area electron diffraction (SAED) pattern of N6 sample revealing its polycrystalline nature.

(B) At low magnification, for the sample N24 (figure 4.16c), the growth of the sheets - most probably by coalescing of the smaller sheets - was observed. The crystalline nature was noticed when higher magnification image was obtained on the representative sheet-like structure (figure 4.16d). The lattice spacing of 0.236 nm corresponded to (110) plane of cubic metallic molybdenum. The SAED pattern of N24 sample (inset of figure 4.16d) disclosed the single-crystalline nature. The slight increase in the d value corresponding to (110) plane of cubic metallic molybdenum for both N6 and N24 samples can be attributed to the presence of native MoO_3. (C) For sample N48, low magnification image (figure 4.16e) illustrated the formation of hierarchical chunk like structures which appeared to be formed due to agglomeration of smaller sheet-like structures. A similar trend was also detected in the FESEM image (figure 4.15e) of the same sample. The polycrystalline structure was revealed at higher magnification (figure. 4.16 f). The lattice spacing ~ 0.201 nm could be indexed as (201) plane of monoclinic MoO_3. The SAED pattern in the inset of the figure 4.16f confirmed the polycrystalline nature of the sample.

4.4.3   Antimicrobial activity study

Microbial infection is a major cause of concern in the medical industry. Biomedical devices, components, and implants are major carriers of such infections. Therefore, as a preventive measure to restrict/eliminate the bacterial colonization, it is imperative to fabricate/coat biomedical devices, components and implants using NCs with ingrained antimicrobial inorganic nanostructured materials. In the proposed assembly of Mo -MoO_3-PPS NCs, PPS can impart the flexibility of extruding it into the desired shape of any biomedical component or implant while entrapped nano-scale Mo-MoO_3 can exert antibacterial action. As a preliminary effort to support our hypothesis, we have performed the study concerning antimicrobial activity of the prepared powders of Mo-MoO_3-PPS NCs. We expect that this study opens up the door for NCs based inorganic pathways to develop bactericidal and fungicidal components and coatings for biomedical industry. The anti-microbial activity of the resultant NCs was studied, and the results revealed that all the NCs acted as excellent antimicrobial agents against both bacteria and fungi. All the NCs exhibited the highest zone of inhibition against *S. aureus*. The inhibition halo diameter was found to be 12, 15 and 17 mm for N6, N24 and N48 NCs, respectively. The zone of inhibition increased with the gradual rise in concentrations of NCs revealed in Table.4.1.

Concentration of Nanoparticles (µg)	Micro-organisms				
	E. coli	*P. aeruginosa*	*S. Aureus*	*K. pneumoniae*	*A. fumigatus*
	Inhibition halo diameter (mm)				
N6					
25	00	00	00	00	00
50	00	00	00	00	00
75	00	00	00	00	00
100	00	00	00	05	00
500	00	06	12	07	09
N24					
25	00	00	00	00	00
50	00	00	00	00	00
75	00	00	00	00	00
100	00	00	00	05	00
500	05	06	15	07	09
N48					
25	00	00	00	00	00
50	00	00	00	00	00
75	00	00	00	00	00
100	00	00	00	09	00
500	07	09	17	10	11

Table. 4.1 Zone of inhibition of NCs at different concentrations against the microorganisms

N48 sample exhibited the highest antibacterial activity and the highest antifungal activity as compared to other nanostructured composites used in the present study. Significant zone of inhibition was obtained for the concentration of 500 µg. The higher concentration required for such activity may be attributed to the entrapment of the synthesized nanoparticles within the polymer matrix. An additional aspect of this study was that for concentration of 100 µg, considerable (5 mm-9 mm) inhibition halo diameter was noted for *K. pneumoniae* colony treated with the NCs. *A. fumigates* when treated with the NCs samples displayed zone of inhibition from 9 to 11 mm. **Interestingly, to the best of our knowledge, this is the first report on antifungal activity against *A. fumigatus* using any kind of NCs system.**

a) MIC/MBC/MFC

The MIC/MBC/MFC values for bacterial as well as fungal colonies treated with NCs samples were provided in Table 4.2. Since, MIC (data not shown) and MBC/MFC values (Table 4.2) for all the samples and concentrations

matched with each other, the formulations of NCs were considered to be bactericidal /fungicidal. The maximum sensitivity towards MBC values (0.8 mg/ml) was recorded for sample N48 in all the bacterial cultures. However, sample N24 has also induced similar sensitivity in *P. aeruginosa, S. aureus, and K. pneumoniae*. Curiously, MFC value for *A. fumigates* is noted to be 1.5 mg/ml.

Microorganism	Concentration mg/ml		
	Sample code		
	N6	N24	N48
P. aeruginosa	1.0	0.8	0.8
S. aureus	1.0	0.8	0.8
E. coli	1.0	1.0	0.8
K. pneumoniae	1.0	0.8	0.8
A. fumigatus	1.5	1.5	1.5

Table 4.2 *MBC/MFC determination of NCs against the microorganisms.*

The antimicrobial activity of NCs was striking, especially, because there are no reports associated with metal/metal oxide nanostructures embedded within the polymer matrix and still exhibiting antimicrobial activity. However, Ana M. Díez- Pascual et al. studied the antibacterial activity on ZnO-PPS NCs [36]. It may be noted that bare nanoparticles always exhibit higher MBC/MFC values at lower concentration, but their application can be limited owing to their potential cytotoxicity, mixing with body fluids and lack of platform. Coating of such nanoparticles on biomedical devices and components is also tedious, expensive and rigid. However, such drawbacks can be overcome in the case of polymer NCs but at the cost of lower MBC/MFC values at a lower concentration.

b) Time-kill assay

Since NCs sample N48 has revealed maximum antibacterial activity, it was allotted for time kill assay against *Staphylococcus aureus*. The cells of *S. aureus* exhibited different growth curve patterns when exposed to the different concentrations of N48 NCs as illustrated in the figure 4.17. In this investigation, for control as well as sub-inhibitory concentration (½ MIC), lag phase ended at 6h and log phase lasted up to 16h. Subsequent to this, steady state growth was noted. However, the degree of growth was found to be smaller for sub-inhibitory concentration. Nonetheless, at inhibitory concentrations i.e. MIC and 2 × MIC, least to no growth was observed till

10h implying that significant delay occurred before the initiation of log phase. During the log phase (10-14h), very small scale growth was observed. Thus, it can be concluded that inhibitory concentrations caused drastic growth inhibitions and consequently can be used as antibacterial biomedical components. It is speculated that release of Mo^{2+} ions from Mo as well as MoO_3 lead to the killing of bacterial cells presumably by disruption of the cell wall.
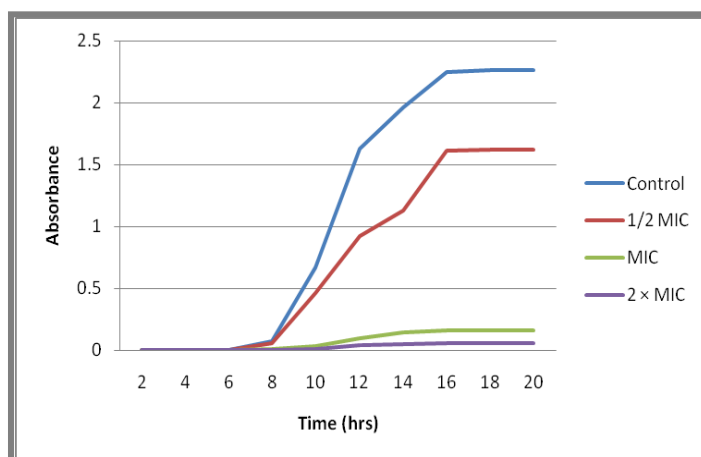
Figure 4.17 Kill-Growth (time) curves of Staphylococcus aureus cells exposed to different concentrations of N48 NCs.

4.4.4 Summary

Solid-solid reaction protocol involving $MoCl_3$ and PPS for the synthesis of Mo-MoO_3-PPS NCs was developed. Metallic Mo was noted to be the dominant phase. As the reaction proceeds from 6h to 48h on time-scale, the tendency to generate $MoO_3$was found to be enhanced. The synthesized NCs were subjected to antimicrobial activity by determining MBC/MFC and time kill curves. The higher concentration of the NCs required for attaining the antimicrobial activity may be attributed to the entrapment of the synthesized nanostructures within the polymer matrix which can hamper the direct exposure of an active surface area of nanoparticles to microbial cells. However, this work is significant as it unlocks the prospectus of fabricating the biomedical devices and components (or coating on them) using such antimicrobial NCs. The preliminary results of antifungal activity are indicative of the fact that these materials can potentially demonstrate anti-cancer properties as it is a thumb rule that antifungal materials are also anti-carcinogenic in nature. More investigations in this direction are underway.

4.5 Overall Conclusions

Solid-solid reaction protocols involving different molybdenum precursors and PPS for the synthesis of Mo-MoO$_3$-PPS and MoO$_3$–PPS NCs were developed. MoO$_3$-PPS NCs were obtained when ammonium molybdate and molybdenum hexacarbonyl were used as Mo precursors. Investigations on dielectric properties are the salient aspect of this work which reveals better dielectric constant and appreciable loss tangent values for the resultant nanocomposites which were prepared using molybdenum hexacarbonyl. The first envisaged application for these nanocomposites may be capacitors for high power, high temperature (up to 125 °C) AC field and surface mount circuits. Mo-MoO$_3$-PPS NCs were obtained when molybdenum chloride was used as Mo precursor. Mo-MoO$_3$-PPS NCs synthesized by MoCl$_3$ as Mo precursor were subjected to antimicrobial activity by determining MBC/MFC and time-kill curves. The preliminary results of antimicrobial investigations indicated promising results regarding preparation of anti-carcinogenic drugs as well as fabrication of the biomedical devices and components using such antimicrobial NCs. The summary of the experimental results obtained from this chapter as tabulated in Table 4.3:

Mo precursor	Polymer	Temperature	Structure	Morphology	Applications
Ammonium molybdate	PPS	285° C	MoO$_3$-PPS NCs	Spherical, irregular, nanorods, sheets, cubic block and rectangular brick	-
Molybdenum hexacarbonyl	PPS	285° C	MoO$_3$-PPS NCs	Irregular, rod, strip, and sheets	Dielectric properties
Molybdenum chloride	PPS	285° C	Mo-MoO$_3$-PPS NCs	Rods, sheets, spherical and irregular	Antimicrobial activity.

Table 4.3 *The summary of the experimental results obtained.*

References

[1] Royer S. and Duprez D. (2011) "Catalytic oxidation of carbon monoxide over transition metal oxides" *Chem. Cat. Chem.* 3:24–65.

[2] Meyer J., Hamwi S., Kröger M., Kowalsky W., Ried T. and Kahn A. (2012) "Transition metal oxides for organic electronics: energetics, device physics and applications" *Adv. Mater.* 24: 5408–5427.

[3] Deng W., Ji X., Chen Q. and Banks C. E. (2011) "Electrochemical capacitors utilising transition metal oxides: an update of recent developments" *RSC Adv.* 1: 1171-1178.

[4] Poizot P., Laruelle S., Grugeon S., Dupont L. and Tarascon J. M.(2000) "Nano-sized transition-metal oxides as negative-electrode materials for lithium-ion batteries" *Nature* 407:496-499

[5] Yuan C., Wu H. B., Xie Y. and Wen (David) Lou X. (2014) "Mixed transition-metal oxides: design, synthesis, and energy-related applications" *Ang. Chem. Int. Ed.* 53:1488–1504.

[6] Soulé J. F., Miyamura H. and Kobayashi S. (2011) "Powerful amide synthesis from alcohols and amines under aerobic conditions catalyzed by gold or gold/iron, -nickel or -cobalt nanoparticles" *J. Am. Chem. Soc.*133 (46):18550–18553.

[7] Chen J., Liu J., Fang Z. and Zeng L. (2011) "Random dsDNA-templated formation of copper nanoparticles as novel fluorescence probes for label-free lead ions detection" *Chem. Commun.* 48(7):1057–1059.

[8] Lunk H. J., Hartl H., Hartl M. A., M. Fait J. G., Shenderovich I. G., Feist M., Frisk T. A., Daemen L. L., Mauder D., Eckelt R. and Gurinov A. A. (2010) "Hexagonal molybdenum trioxide known for 100 years and still a fount of new discoveries" *Inorg. Chem.* 49:9400–9408.

[9] Dong W., Huang H., Zhu Y., Li X., Wang X., Li C., Chen B., Wang Ge. and Shi Z. (2012) "Room-temperature solution synthesis of Ag nanoparticle functionalized molybdenum oxide nanowires and their catalytic applications" *Nanotechnology.* 23:425602.

[10] Song L. X., Wang M., Pan S. Z., Yang J., Chen J. and Yang J. (2011) "Molybdenum oxide nanoparticles: preparation, characterization, and application in heterogeneous catalysis" *J. Mater. Chem.* 21:7982– 7989.

[11] Bai S., Chen S., Chen L., Zhang K., Luo R., Li D. and Liu C. C. (2012) "Ultrasonic synthesis of MoO_3 nanorods and their gas sensing properties" *Sensors and Actuators B: Chemical.* 174:51–58.

[12] Afanasiev P., Xia G.F., Berhault G., Jouguet B. and Lacroix M. (1999) "Surfactant-assisted synthesis of highly dispersed molybdenum sulfide" *Chem. Mater.* 11:3216–3219.

[13] Tan K. S., Chuang M. K., Chen F. C. and Hsu C. S. (2013) "Solution-processed nanocomposites containing molybdenum oxide and gold nanoparticles as anode buffer layers in plasmonic-enhanced organic photovoltaic devices" *ACS Appl. Mater. Interfaces.* 5:12419–12424.

[14] Close M. R., Petersen J. L. and Kugler E. L. (1999) "Synthesis and characterization of nanoscale molybdenum sulfide catalysts by controlled gas phase decomposition of Mo (CO)$_6$ and H$_2$S" *Inorg. Chem.* 38:1535–1542.

[15] Mdleleni M. M., Hyeon T. and Suslick K. S. (1998) "Sonochemical synthesis of nanostructured molybdenum sulfide" *J. Am. Chem. Soc.* 120:6189–6190.

[16] Bonneau P. R., Jarvis Jr. R. F. and Kaner R. B. (1991) "Rapid solid-state synthesis of materials from molybdenum disulphide to refractories" *Nature* 349:510 – 512.

[17] Zheng L., Xu Y., Jin D. and Xie Y. (2011) "Polyaniline-intercalated molybdenum oxide nanocomposites: simultaneous synthesis and their enhanced application for supercapacitor" *Chemistry – An Asian J.* 6:1505–1514.

[18] Lee S. H., Kim Y. H., Deshpande R., Parilla P. A., Whitney E., Gillaspie D. T., Jones K. M., Mahan A. H., Zhang S. and Dillon A. C. (2008) "Reversible lithium-ion insertion in molybdenum oxide nanoparticles" *Adv. Mater.* 20:3627–3632.

[19] Krishnamoorthy K., Premanathan M., Veerapandian M. and Kim S. J. (2014) "Nanostructured molybdenum oxide-based antibacterial paint: effective growth inhibition of various pathogenic bacteria" *Nanotech.* 25: 315101.

[20 Murdoch M., Waterhouse G. I. N., Nadeem M. A., Metson J. B., Keane M. A., Howe R. F., Llorca J. and Idriss H. (2011) "The effect of gold loading and particle size on photocatalytic hydrogen production from ethanol over Au/TiO$_2$ nanoparticles" *Nature Chem.* 3:489- 492.

[21] Chan S. C. and Barteau M. A. (2005) "Preparation of highly uniform Ag/TiO$_2$ and Au/TiO$_2$ supported nanoparticle catalysts by photodeposition" *Langmuir* 21(12):5588–5595.

[22] Fageria P., Gangopadhyay S. and Pande S. (2014) "Synthesis of ZnO/Au and ZnO/Ag nanoparticles and their photocatalytic application using UV and visible light" *RSC Adv.* 4:24962-24972.

[23] Kango S., Kalia S., Celli A., Njuguna J., Habibi Y. and Kumar R. (2013) "Surface modification of inorganic nanoparticles for development of organic–inorganic nanocomposites—a review" *Prog. Poly. Sci.* 38:1232–1261.

[24] Xia X., Hao Q., Lei W., Wang W., Wang H. and Wang X. (2012) "Reduced-graphene oxide/molybdenum oxide/polyaniline ternary composite for high energy density supercapacitors: Synthesis and properties" *J. Mater. Chem.* 22: 8314.

[25] Xie L., Huang X., Wu C., and Jiang P. (2011) "Core-shell structured poly(methyl methacrylate)/BaTiO$_3$ nanocomposites prepared by *in-situ* atom transfer radical polymerization: a route to high dielectric constant materials with the inherent low loss of the base polymer" *J. Mater. Chem.* 21:5897.

[26] Zhou J., Xu N. S., Deng S Z., Chen J., She J. C. and Wang Z. L.(2003) "Large-area nanowire arrays of molybdenum and molybdenum oxides: synthesis and field emission properties" *Adv. Mater*. 15:1835-1840.

[27] Hong S. Y., Popovitz-Biro R, Prior Y and Tenne R (2003) "Synthesis of Sns$_2$/Sns fullerene-like nanoparticles: a superlattice with polyhedral shape" *J. Am. Chem. Soc.* 125:10470-10474.

[28] Rumale N., Arbuj S., Umarji G., Shinde M., Mulik U., Pokle A., Hawaldar R. and Amalnerkar D. (2013) "Thermoplastic polymer domain for synthesis of manganese sulphide nanoparticles by simple solid-solid reaction" *Nanosci. Nanotech. Lett.* 5:902-906.

[29] Rumale N., Arbuj S., Umarji G., Shinde M., Mulik U., Pokle A., Shinde S. and Amalnerkar D. (2013) "*In-situ* fabrication of cobalt oxide / sulphide mixed phase nanoparticles in Polyphenylene Sulphide matrix" *Carbon Sci. Tech*. 5(2): 243-250.

[30] Rumale N., Arbuj S., Umarji G., Shinde M., Mulik U., Pokle A. and Amalnerkar D. (2013) "Simplistic approach for *in-situ* generation of ZnS quantum dots in polyphenylenesulphide matrix via chalcogen enriched solid-solid reaction technique" *Phys. Status Solidi. A*. 210:345-348.

[31] Rumale N., Arbuj S., Umarji G., Shinde M., Mulik U., Pokle A. and Amalnerkar D. (2013) "Single step solid-solid reaction scheme for the synthesis of cobalt sulphide-oxide nanoparticles in polymer matrix" *Adv. Nanopar*. 2: 28-31.

[32] Liang R., Cao H. and Qian D. (2011) "MoO$_3$ nanowires as electrochemical pseudocapacitor materials" *Chem. Commun*. 47: 10305.

[33] Techtron$^®$ PPS Materials Notes, Private circulation, http://www.professionalplastics.com/.

[34] Kanade K., Hawaldar R., Mulik U., Kale B., and Amalnerkar D. (2007) "Synthesis of CdS nanocrystallites in polymer matrix: sui-generis approach" *Solid State Phenomena* 119: 21.

[35] Qureshi N., Umarji G., Shinde M., Rane V., Borde L., Mulik U. and Amalnerkar D. (2013) "Innate approach for fabrication of nickel oxide nanocomposite in pellet form and their electric properties" *Mater. Exp.* 3: 79-84.

[36] Pascual A. and Vicente A. (2014) "High performance aminated poly(phenylene sulfide)/ZnO nanocomposites for medical applications" *ACS Appl. Mater. Interfaces.* 6:10132–10145.